Electronic Supplementary Information:

# Mechanical phenotyping of breast cell lines by in-flow deformation-dependent dynamics under tuneable compressive forces

David Dannhauser,†[a] Maria Isabella Maremonti,†[a] Valeria Panzetta,[a] Domenico Rossi,[b] Paolo Antonio Netti[ab] and Filippo Causa*[a]

[a]*Interdisciplinary Research Centre on Biomaterials (CRIB) and Dipartimento di Ingegneria Chimica, dei Materiali e della Produzione Industriale, Università degli Studi di Napoli "Federico II", Piazzale Tecchio 80, 80125 Naples, Italy.*
[b]*Center for Advanced Biomaterials for Healthcare@CRIB, Istituto Italiano di Tecnologia, Largo Barsanti e Matteucci 53, 80125 Naples, Italy.*
*†These authors contributed equally to this work.*
**Correspondence and request for material should be addressed to F.C. (email: filippo.causa@unina.it)*

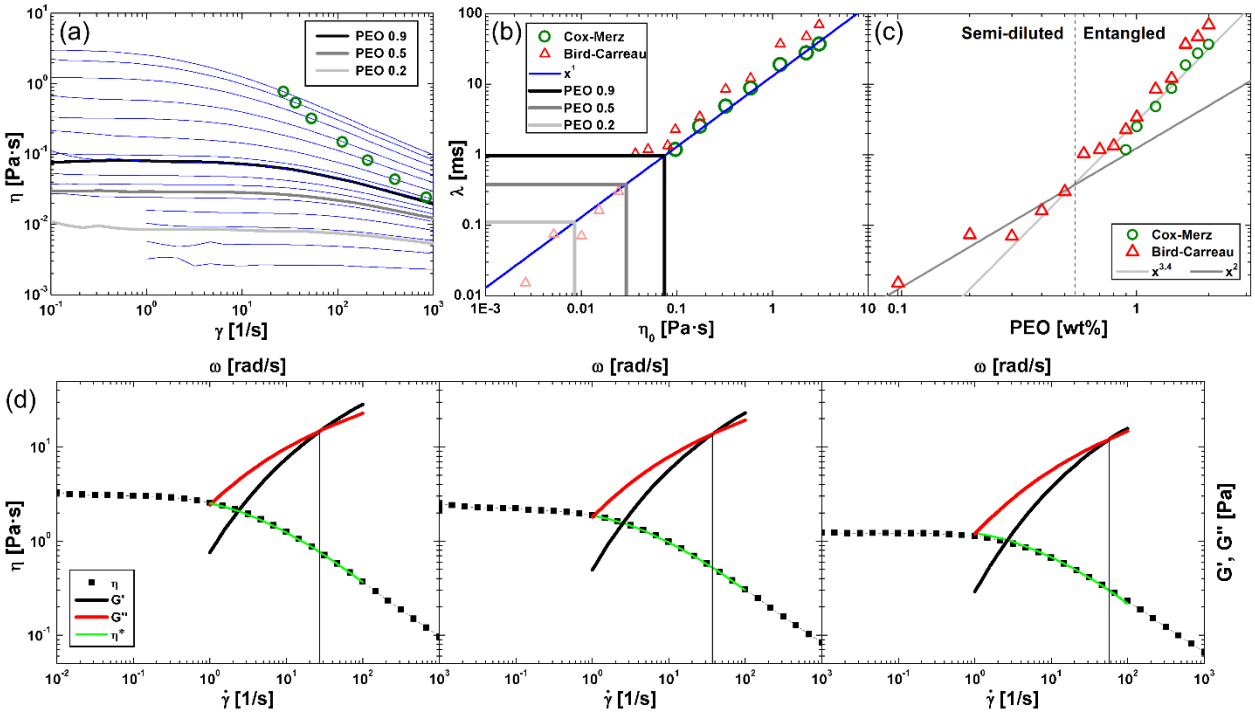


**Fig. S1** Rheological fluid investigations. (a) Shear-rate-dependent ($\dot{\gamma}$) measurements of the fluid viscosity ($\eta$) for a wide range of polyethylene oxide (PEO, 4MDa, Sigma Aldrich) solutions. We highlighted PEO 0.9 (black), 0.5 (grey) and 0.2 (light grey), which correspond to following polymer concentration 0.88, 0.53 and 0.22 wt%, respectively. Green circles indicate the obtained fluid relaxation times ($\lambda$) based on the Cox-Merz approach, where shear-thinning behaviour gets significant.[1] In particular, $\eta$ values (including the complex viscosity $\eta^*$) of the crossing point between storage ($G'$) and loss ($G''$) modulus (shown in d) are related to $\eta_0$ values for high PEO concentration (2.0, 1.8 and 1.6 wt%). The hereby calculated median decrease of $\eta$ value was applied on further PEO concentration (1.4, 1.2, 1.0, 0.9 wt%), where no crossing point between $G'$ and $G''$ can be obtained by the used standard Rheometer approach, until $\eta$ values are out of measurement range. Parallel analysis using the Bird-Carreau fitting[1] of the obtained $\eta$ curves indicated similar $\lambda$ outcome (results shown in b by red triangles). (b) $\lambda$ versus $\eta_0$ are plotted for the Cox-Merz and the Bird-Carreau approach, showing similar outcome. The PEO concentrations of interest are highlighted as followed: PEO 0.9 (black), 0.5 (grey) and 0.2 (light grey). A direct relationship between $\lambda$ versus $\eta_0$ was obtained. Therefore, any possible value of $\eta_0$ can be related to a $\lambda$ value. (c) The entanglement concentration (c* = 0.56 wt%)[2], between semi-dilute unentangled regime and entangled regime is indicated. The change of diluted to semi-diluted regime is expected at a PEO concentration of ~0.2 wt%. (d) Flow curve results of $\eta$ versus $\dot{\gamma}$ are plotted for PEO 2.0, 1.8 and 1.6 wt% with overlaid frequency sweep outcome for $G'$, $G''$ and $\eta^*$ to obtain the crossing point with $\eta$. Out of these measurements $\lambda$ of the PEO solution is measured. Data was obtained using a stress-controlled rheometer (MCR302, Anton Paar) with cone-plate (diameter of 50mm) geometry. Note that all values of $\lambda$ represent the rheological properties of the viscoelastic liquid, without the presence of cells or rigid particles.

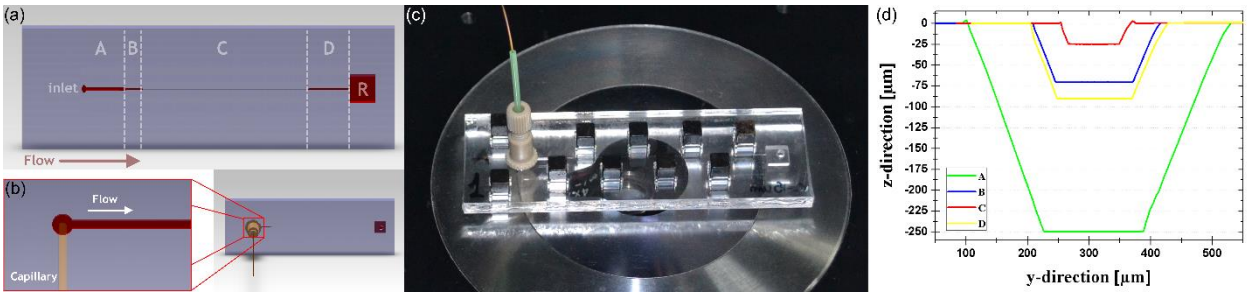


**Fig. S2** Microfluidic chip design. (a) Design of inlet, reservoir (R) and different rectangular shaped cross-sections (A, B, C and D) of the main chip part are illustrated without cover. (b) Chip with closed cover, capillary tube and fluid connector is shown without magnets. The zoom-out indicate the capillary tube position at the inlet of the chip, with faded out fluid connector for better readability. (c) Assembled microfluidic chip with magnets to hold the cover part in position is presented. (d) Optical surface profilometer (Dektak 150, Veeco) outcome of fabricated microfluidic chip sections. We designed the microfluidic sections of different nominal height and width (A=250x500, B=70x200, C=25x100 or D=90x200 µm, respectively) and measured the sections at the beginning of each section in flow direction. Surface analysis show very precise fabrication stability in vertical direction (channel height), while in horizontal direction (channel width) some imprecision can be noticed due to the profilometer tip geometry (2.5 µm tip radius with 45° cone shape).

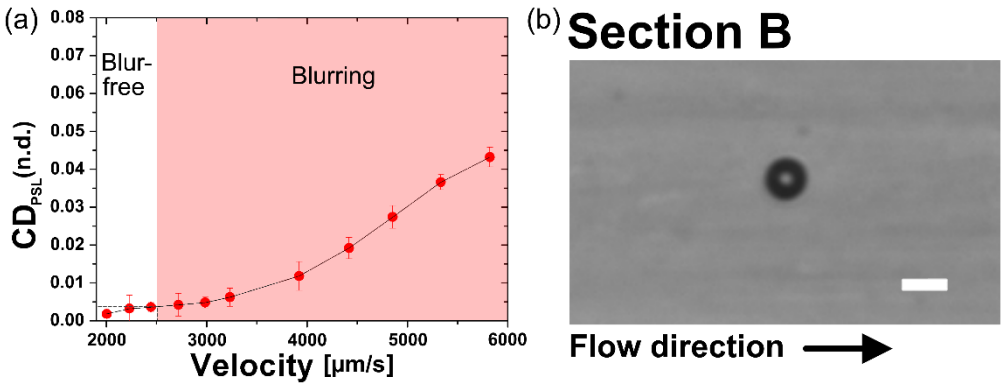


**Fig. S3** Polystyrene beads measurements at different fluid velocities. (a) Cell deformation versus particle velocity is plotted. The highlighted red area indicates *CD* values, for PSL particles, above 0.01, which are considerate as blurring (n>10 for each data point). Therefore, cell measurements should be performed below 2500 µm $s^{-1}$ for the used camera settings (1000 fps, ET<5 ms). Error bars are presented as standard deviation of the mean. (b) An image of a polystyrene bead without blurring effect is presented.

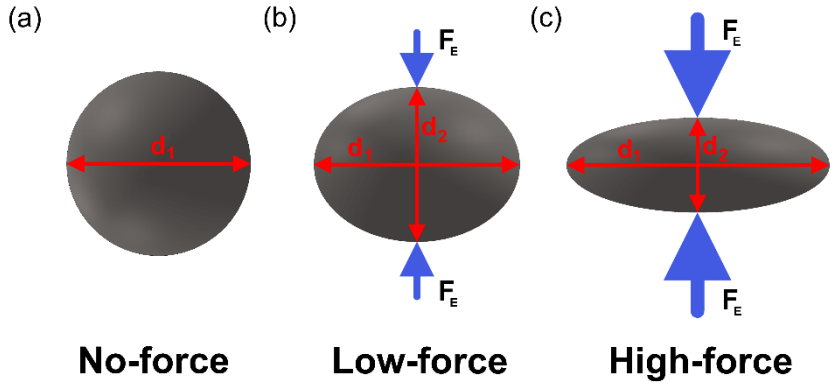


**Fig. S4** Cell deformation sketch for different applied compressive forces at constant initial cell properties. (a) No applied force in-flow, result in an undeformed cell shape and a cell can be defined with a unique diameter $d_1$, as a sphere. Low (b) and high (c) entities of applied forces result in a measurable change of the investigated cell shape and a cell can be defined with minor ($d_2$) and major ($d_1$) axis diameters

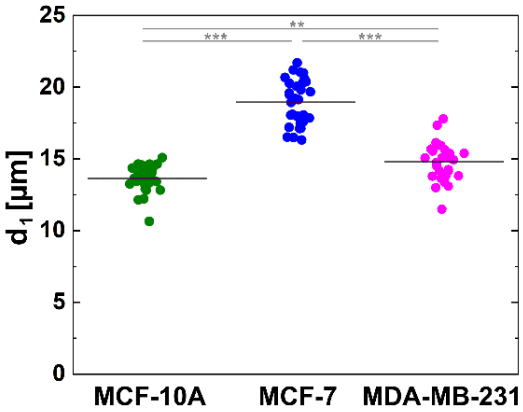


**Fig. S5** Values of cell diameters ($d_1$) observed at confocal microscope at Q. Diameters are plotted for each single cell line (n= 30, 30 and 30 for MCF-10A, MCF-7 and MDA-MB-231, respectively). The mean value of each distribution is indicated by a grey horizontal line. Statistical significances were determined by one-way ANOVA and Tukey's test ($^{ns}p > 0.05$; *p < 0.05; **p < 0.01; ***p < 0.001).

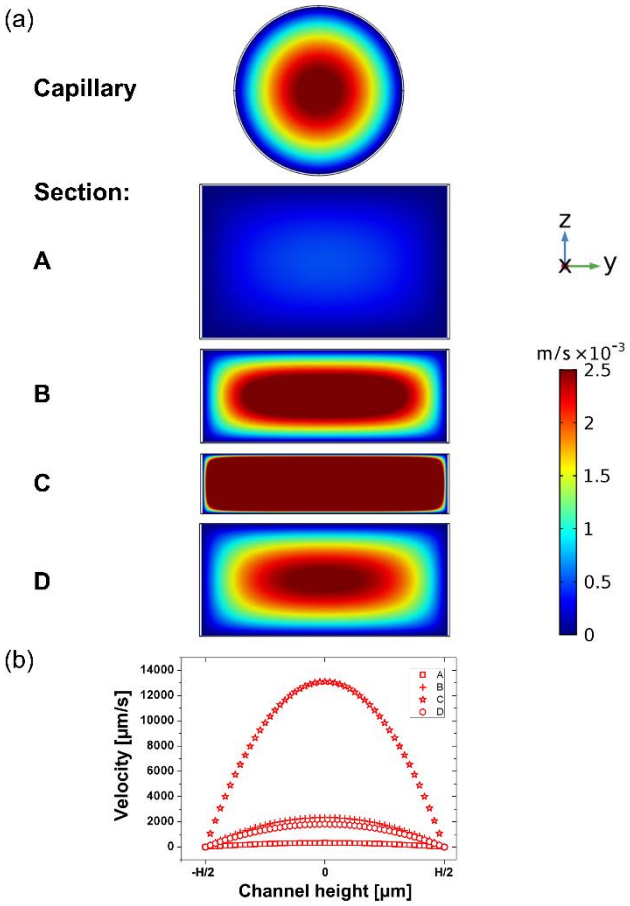


**Fig. S6** Velocity profile simulations of the microfluidic chip sections. (a) Representative velocity distribution for all sections of the microfluidic chip and the inlet capillary are reported in sequent fluid flow order from the top to the bottom. All simulations were calculated using a PEO 0.9 and an applied pressure ΔP= 800 mbar and a capillary R=75 µm. All of the sections were simulated using the Multiphysics 5.3a package COMSOL. (b) Velocity profile over channel height for each channel section is presented, using a self-written Matlab R2019a routine, showing the parabolic Poiseuille fluid flow condition for all sections.

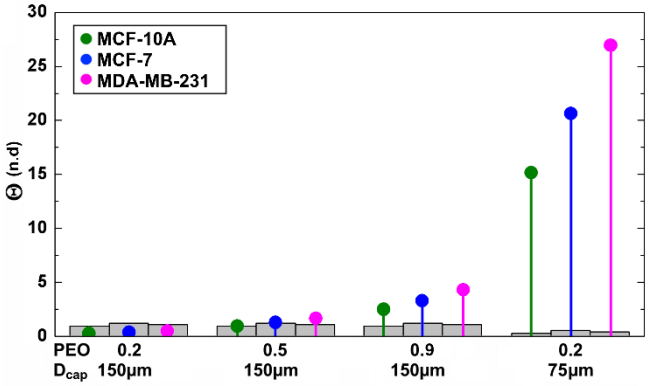


**Fig. S7** Cell alignment probability (Θ) for viscoelastic liquid and cell classes. The grey bars indicate the threshold $(-ln\ (3.5\beta))^3$ to ensure cell alignment. In cases of insufficient cell alignment, the capillary diameter ($D_{cap}$) was reduced from 150 to 75 µm (last case on the right).

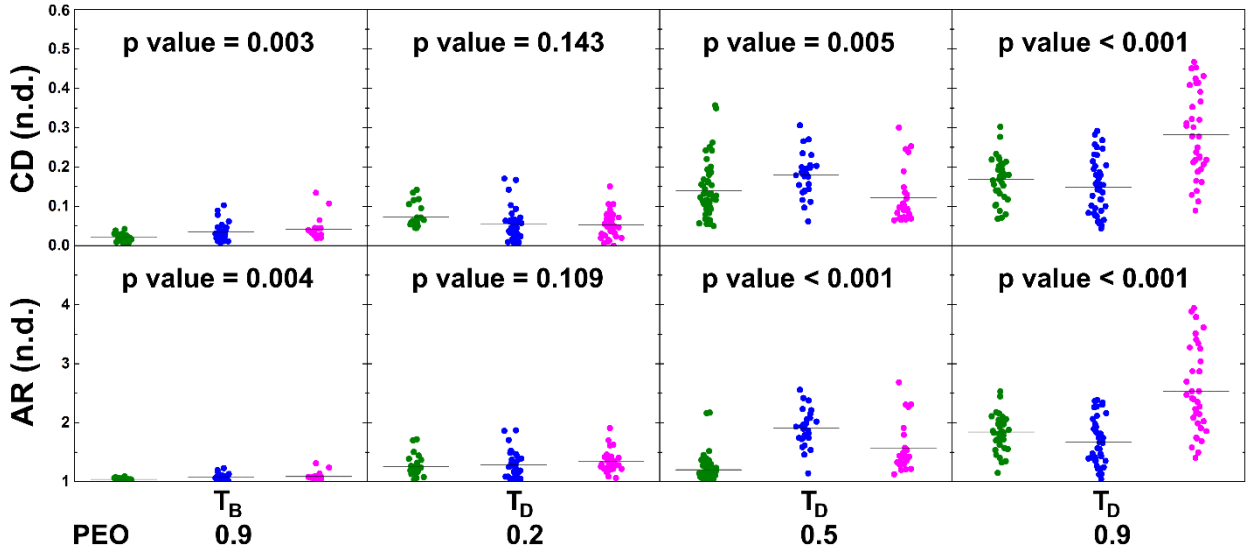


**Fig. S8** Mean values and corresponding distribution of *CD* versus *AR* for each measurement condition. Cell parameter outcome of *CD* and *AR* are plotted before- ($T_B$ - PEO 0.9, with n=31, 29 and 19) and after low- ($T_D$ - PEO 0.2, with n=25, 33 and 35), intermediate- ($T_D$ - PEO 0.5, with n=50, 28 and 27) or high- ($T_D$ - PEO 0.9, with n=35, 42 and 35) entities of in-flow applied $F_E$ for MCF-10A, MCF-7 and MDA-MB-231, respectively. The mean value of each distribution is indicated by a grey horizontal line. Statistical significances were determined by multiple ANOVA between the cell lines.

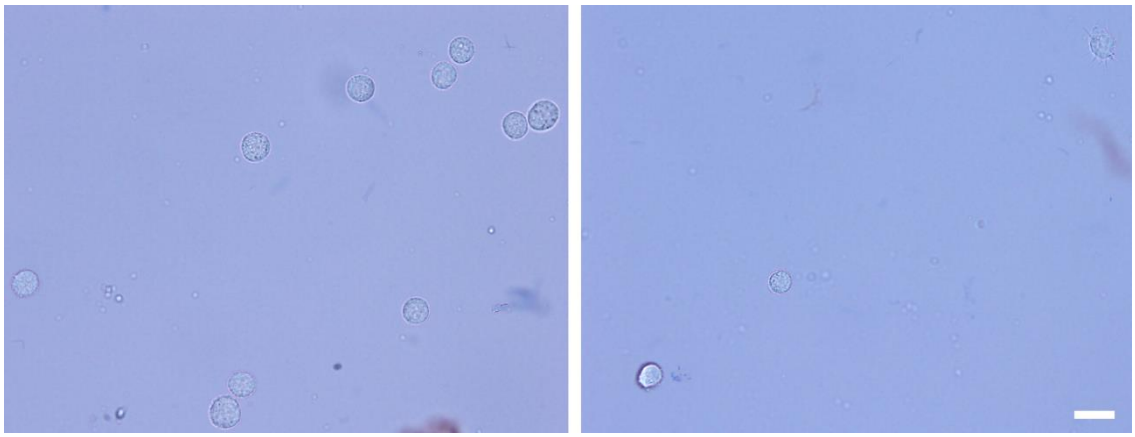

**Fig. S9** Trypan blue test on MCF-7 cells before (left - Q) and after (right - $T_E$) deformation in flow. Length of the scale bar is 20µm.

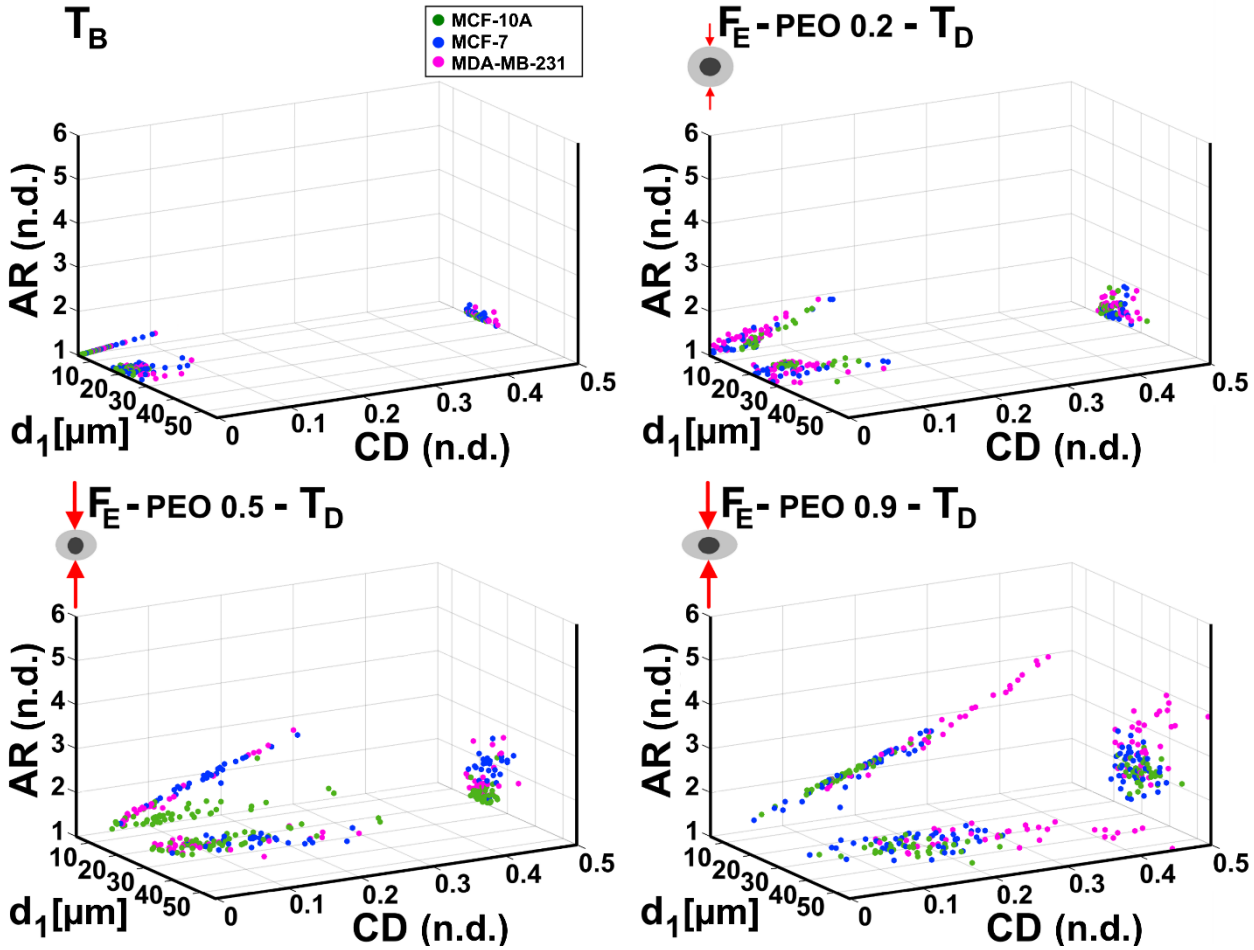


**Fig. S10** Mechanical cell properties investigated by different $F_E$ entities. (a) Cell parameters of interest (*AR*, *CD* and $d_1$) are plotted in a 3D-scatter plot before- ($T_B$ - PEO 0.9, with n=31, 29 and 19) and after low- ($T_D$ - PEO 0.2, with n=25, 33 and 35), intermediate- ($T_D$ - PEO 0.5, with n=50, 28 and 27) or high- ($T_D$ - PEO 0.9, with n=35, 42 and 35 for MCF-10A, MCF-7 and MDA-MB-231, respectively) entities of in-flow applied $F_E$. Note, only the projections surfaces of the 3D-scatter plot are shown for better readability of the plots.

**Table S1** Mean values and standard errors of the measured major diameters of cells ($d_1$) , aspect ratio ($AR$) and cell deformation ($CD$), observed at confocal microscope at Q (n=30, 30 and 30 for MCF-10A, MCF-7 and MDA-MB-231, respectively).

| Cell Type | $\boldsymbol{d_1}[\mu m]$ | $\boldsymbol{AR}$ (n. d.) | $\boldsymbol{CD}$ (n. d.) |
|---|---|---|---|
| MCF-10A | 13.634 ± 0.168 | 1.054 ± 0.005 | 0.021 ± 0.001 |
| MCF-7 | 18.959 ± 0.289 | 1.049 ± 0.005 | 0.017 ± 0.001 |
| MDA-MB-231 | 14.798 ± 0.240 | 1.076 ± 0.008 | 0.018 ± 0.001 |

## References


1 R. B. Bird, R. C. Armstrong and O. Hassager, Dynamics of polymeric liquids. Vol. 1: Fluid mechanics. Wiley-VCH Verlag GmbH & Co, Weinheim, Germany, 1987.

2 F. Del Giudice, G. D'Avino, F. Greco, I. De Santo, P. A. Netti and P. L. Maffettone, Rheometry-on-a-chip: measuring the relaxation time of a viscoelastic liquid through particle migration in microchannel flows. *Lab Chip*, 2015, **15**, 783-792.

3 G. Romeo, G. D'Avino, F. Greco, P. A. Netti and P. L. Maffettone, Viscoelastic flow-focusing in microchannels: scaling properties of the particle radial distributions, *Lab Chip*, **13**, 2802-2807.